In-Flight Imaging of Aerosol Jet Printer Droplets to Enable Spatially Resolved Flow Rate Measurements

Anna Meredith[1], Matthias Beuting[1], Mario Trujillo[1], Scott Sanders[1], Joseph Andrews[1,2,*]

[1] Department of Mechanical Engineering, University of Wisconsin-Madison, Madison, USA
[2] Department of Electrical and Computer Engineering, University of Wisconsin-Madison, Madison, USA

* joseph.andrews@wisc.edu

Abstract

The effect of process drift in aerosol jet printing has been a hindering factor in its large-scale adoption in printed electronics. In this study, we developed an in-situ droplet imaging system using a double-pulse laser to quantify the distribution and velocity of sparse droplets between the aerosol jet printer nozzle and the substrate. The droplet velocity and distribution were then used to evaluate a spatially resolved droplet flow rate that was capable of detecting and quantifying process drift over time. Using the droplet imaging system, the effect of different focus ratios was analyzed. The droplet flow rate was shown to be indicative of the deposited line morphology for low to moderate focus ratios. At a high focus ratio, the tool was able to identify non-idealities in the fluid properties which are explained in a detailed analysis. Aerosol jet printing demonstrates significant promise for the additive manufacturing of electronics, and this work represents a step towards non-invasive, in-flight monitoring in real-time.

Keywords: aerosol jet printing, focus ratio, printed electronics

1. Introduction

Printed electronics technology offers an attractive method to fabricate large-area and flexible circuits due to its simplicity and versatility, specifically in comparison to traditional lithography-based techniques.[1–6] In general, printed electronic technologies use additive processes to simultaneously deposit and pattern solution-based electronic materials. The technique was first demonstrated in 1936,[7] and since then a range of methods have been developed that can accommodate a variety of inks and substrates.[8–10]

One subset of printing techniques that has gained significant interest is direct-write non-contact methods, such as inkjet and aerosol jet (AJ) printing. In non-contact methods, the standoff distance between the printer and the substrate allows for material deposition onto substrates with complex topographies. Additionally, the digital nature of direct-write processes offers high customizability, enabling efficient electronic prototyping.[11] These techniques, which are particularly well suited for large-area and flexible electronic devices,[2,12,13] have impacted the fields of sensing, displays, and radio identification tag circuitry among others.[14–16]

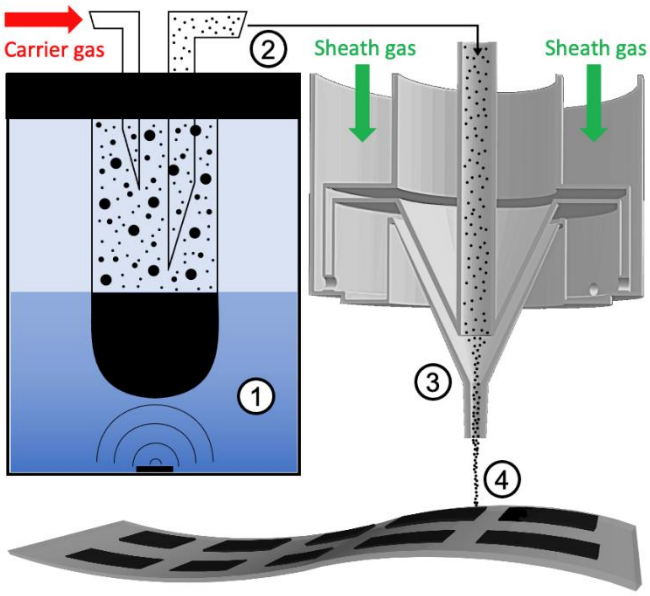

Figure 1. Schematic diagram of the AJ printing process broken up into four key steps, 1) aerosol generation through ultrasonic atomization, 2) aerosol transport from the atomizer to the deposition head using an inert carrier gas, 3) aerodynamic focusing of the aerosol stream using an inert sheath gas, 4) impingement of the aerosol droplets on the substrate.

AJ printing offers non-contact printing with substantial substrate standoff distances (10 mm) and noteworthy compatibility with many ink rheologies.[17–19] The large stand-off distance allows for printing onto substrates with topographical inclines up to 70° without tilting the nozzle.[20] The first step in AJ printing is the transformation of liquid ink into an aerosol that can be focused and deposited using an inert gas. A common method to generate the aerosol is through ultrasonication, in which sonically generated capillary waves within the bulk fluid cause droplets on the order of 0.5–5 µm to be ejected.[21,22] These droplets are carried by an inert carrier gas through transport tubing. Once the aerosol has reached the deposition head, a co-annular flow of inert gas, known as the sheath gas, enters the fluid stream to focus the aerosol before the aerosol exits the nozzle and deposits on the substrate. This focusing gas allows for high-resolution printing, with line widths approaching 5 µm, while simultaneously protecting the nozzle from clogging.[18] A schematic description of the process is shown in Figure 1.

Although AJ technology can facilitate the printing of high-resolution circuitry on complex geometries, AJ printing is yet to be fully utilized in large-scale production due to its limited reproducibility. One factor that affects the reproducibility is the reduction of ink volume over time, which has been investigated and improved in previous work by Tafoya *et al.*[23] In addition to the reduction in ink quantity, the ink quality can also decrease due to preferential aerosolization of one or more of the materials in the ink. The change in ink quality can cause deviations in the size and composition of the droplets. Another factor is the material impingement on the walls of the transport tube and within the nozzle. The accumulation of this material leads to a decrease in the space available for droplets to travel through, increasing droplet velocity. These deviations affect the deposited material morphology and are known in the field as process drift.

Commonly, the process control is purely open-loop, where the user selects parameters for the ink temperature, the ultrasonication power, the sheath and carrier gas flow rates, the platen speed, and the platen temperature. To combat drift in the process and improve consistency, several attempts to achieve closed-loop printing using a number of feedback techniques have been reported in the literature. Salary *et al.* utilized the online process camera, which provides real-time visual feedback of the ink deposition, enabling online monitoring of line width.[18,24] Through direct control of the platen speed, the authors were able to maintain some consistency in line width. However, this method does not ensure consistency in line thickness or overall material density, which can severely affect electrical performance.

In another work, Tafoya *et al.* used optical absorption measurements within the transport tube to calculate the total droplet loading.[25] This measurement correlates with the deposited mass providing robust control of electrical properties within graphene thin films. However, the method does not allow for direct geometric control of the printed features.

Ultimately, a non-invasive feedback mechanism that can enable direct measurements of droplet density, distribution, and flow rate is required to control for both the geometry and electrical properties of printed traces. To address this concern, we have designed and characterized an optical method that uses a pulsed laser system to directly probe the aerosol column properties. A common technique for size, position, and velocity measurements in inkjet printing is the use of stroboscopic pulsed light-emitting diodes.[26] In AJ printing, however, the droplets are significantly faster and smaller, requiring a light source that produces shorter pulses (5–20 ns) at higher intensities. Additionally, our technique allows the droplet field to be captured in a single frame, even when the droplet positions are stochastically distributed across the droplet column. The in-flight imaging system gathers information about the small droplets (0.5–5 µm) traveling at high velocities (10–100 m s^{-1}) which can be used to indicate the line morphology. Due to the size scale of the aerosol droplet column, which can be predicted analytically using ultrasonic theory described elsewhere, the scattering intensity is not directly correlated to droplet size.[27] The light scattering occurs in the Mie regime since the droplet size is on a similar order to the excitation wavelength. Here, the dependence of the measured intensity on the droplet size is non-trivial precluding our technique from providing direct droplet size measurements. To accurately describe the flow of the fluid,

we develop a spatially resolved flow rate. The spatially resolved flow rate was developed based on two key assumptions. First, there will be negligible mixing of the sheath and carrier gases assuming laminar flow of the bulk fluid. Secondly, the velocity of the bulk fluid will be axially symmetric with the sheath gas encasing the carrier gas.[28]

The technique also allows for direct observation of the spatial variation of droplet velocity within the aerosol column. This technique is used to examine the in-flight properties at varied focus ratios *FR*, defined as

$$Eq.1 \qquad \mathrm{FR} = \frac{S}{C}$$

where *S* and *C* are the sheath and carrier gas flow rates, respectively. The focus ratio indicates the degree to which the aerosol column is focused by the sheath gas and has been demonstrated as a preliminary metric for the line quality.[29] Using the in-flight imaging system, the effect of the focus ratio on droplet velocity and distribution between the nozzle and the substrate can be investigated.

2. Experimental

2.1 Aerosol Jet Printing

The experiments were conducted on the Aerosol Jet 200 (Optomec) printer using an aqueous silver nanoparticle ink with 50% loading (JS-A426, Novacentrix). The ink was deposited on glass microscope slides (Globe Scientific) that were sonicated in acetone (Sigma-Aldrich) for 5 min and treated in an ultraviolet ozone cleaner (L2002A3-US, Ossila) for 5 min. For the focus ratio investigation, the carrier gas flow rate was maintained at 30 SCCM, while the sheath gas flow rate was adjusted according to Eq. 1. In all experiments, a 200 μm nozzle (Optomec) was used. In all cases, the standoff distance between the nozzle and the substrate was 6 mm. However, the substrate and the platen were removed from the droplet stream for the "at the substrate" data set to prevent the interference of reflected light from the substrate in the droplet images. For comparison between the in-flight and impinged droplet flow rates over time, the AJ printer flow rates were set to 20 and 40 SCCM for the carrier gas and sheath gas respectively. 500 in-flight images were collected at a rate of 10 fps. Sparse droplets were printed using a platen speed of 200 mm s^{-1}. In the focus ratio investigation, dense lines were printed using a platen speed of 1 mm s^{-1}. Nitrogen was used as both the carrier gas and the sheath gas.

2.2 In-Flight Imaging

The imaging system consists of a laser illuminating the droplet stream and a camera with magnification optics to detect the light scattered from the droplets (Figure 2). Besides precise timing control, the laser provides sufficient fluence to allow observation of droplets smaller than the resolution limit of the optical detection system. The measured optical signal stems from the incident light scattered by the liquid droplet. Therefore, while we present images related to silver nanoparticle-laden aqueous ink, we expect this technique to apply to non-aqueous inks of varied particle loading, including inks consisting of metal-organic precursors.

The detection side comprises a complementary metal-oxide semiconductor (CMOS) camera (PL-D752CU-T, Pixelink), a focal length f = 200 mm tube lens with optical zoom (Optem FUSION 1X with 12.5:1 zoom module, QIOPTIQ), and a far-field microscope objective (10X M Plan Apo, Mitutoyo) with a 34 mm working distance. At the zoom settings used for all experiments, the field of view was 730 by 1160 μm. The focal plane in the center of the droplet stream was approximately 150 μm thick in the direction of view. The optical resolution was 228 line pairs per mm. The droplets are illuminated using a frequency-doubled dual-cavity Nd:YAG laser (Solo PIV 120, New Wave Research) emitting at a wavelength of 532 nm and a pulse width of 5 ns. The laser beam is formed into a thin (<250 μm) light sheet using a f = 500 mm cylindrical lens. The energy per pulse is attenuated to <15 mJ to avoid excessive heating of the droplets and saturation of the camera sensor. The timing of the camera and the laser pulses is controlled by a digital delay/pulse generator (DG535, Stanford Research Systems). The camera exposure time was set to 100 ms at a gain of 24 dB. Within the exposure time, two laser pulses with a 500 ns delay are emitted.

2.3 Image Processing

The 5 ns pulses emitted by the laser illuminate the droplets at their initial (pulse one) and final (pulse two) positions. Both illuminations are captured by a single camera exposure. Using the known delay between the two laser pulses, the droplet velocity can be calculated. To automate this process, an image processing algorithm was developed to pair the droplets and extract information about the aerosol column. The algorithm converts the raw images to grayscale and then to binary using a threshold. The white pixels are grouped with neighboring white pixels to form clusters. The coordinates of the droplets are calculated using the centroid location of the clusters. Droplets are then paired based on their coordinates. An example of the image processing, including the raw, binarized, and paired version of a single frame, is shown in Figure 3.

$$Eq.2 \qquad v_g = \frac{S + C}{\pi r^2}$$

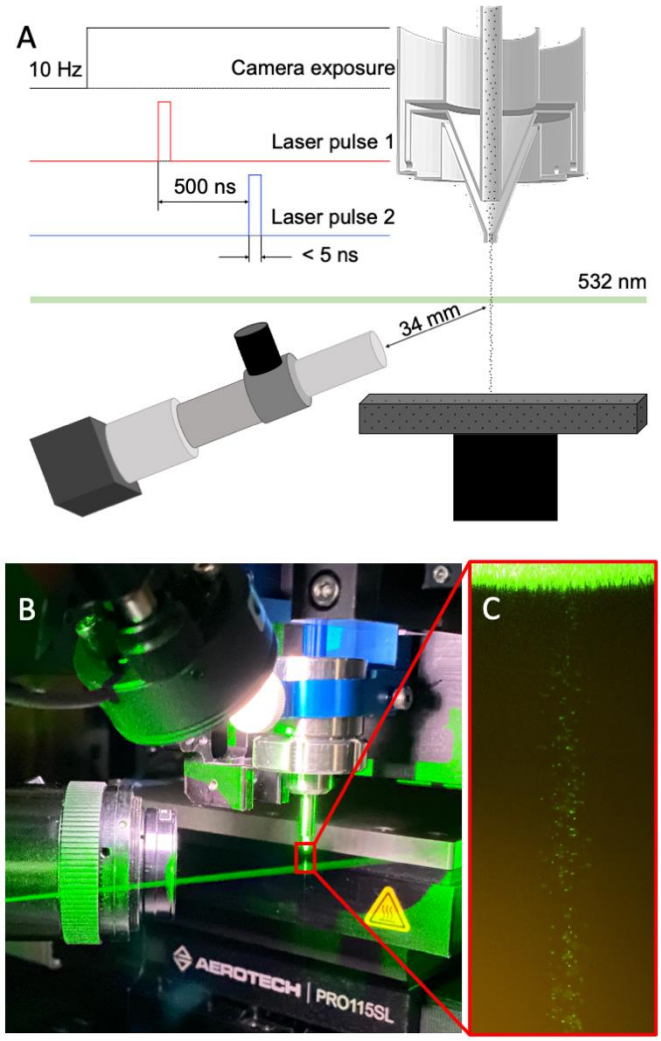

Figure 2. Apparatus setup for obtaining in-flight, droplet-level measurements within an AJ printing system A) schematic depicting the laser pulse measurement system setup including the timing of the camera exposure and laser pulses (not to scale), B) photograph of one variation of the setup in which the aerosol column can be visualized, C) long-exposure image of the droplet column using illumination from the double pulsed laser.

The calculated droplet velocity can be validated against the theoretical overall gas velocity (Eq. 2) based on the assumption that the mass flow rate directly correlates to the volumetric flow rate. The total mass flow rate is equal to the sum of the sheath and carrier gas flow rates, which is then converted to a linear velocity by dividing by the cross-sectional area at the tip of the nozzle. This is shown in Eq. 2, where v_g is the theoretical overall gas velocity and r is the inner radius of the nozzle. This velocity can be used to approximate the droplet velocity and provide insight into the properties of the bulk fluid.

2.4 Characterization

The impinged droplets and the deposited lines were imaged using an optical microscope (Axio Lab.A1, Carl Zeiss). The line heights and widths of the printed traces were determined using an optical profilometer (New View 9000, Zygo). The calculated line width includes all of the deposited material, including overspray, in order to correlate with the in-flight images where there is no differentiation between line and overspray. Prior to profilometry, the samples were coated with 60 nm of platinum using a sputter coater (ACE600, Leica). The in-flight images were processed and analyzed using the algorithm described in section 2.3 implemented in MATLAB (2022b, MathWorks). The impinged droplets used for the in-flight flow rate measurement comparison were counted using ImageJ.

3. Results and Discussion

3.1 In-Flight Flow Rate Measurement

As mentioned in the introduction, our measurement technique is designed to provide information related to the flow rate and spatial distribution of the droplets simultaneously. Assuming the images of the sparse droplets act as snapshots within time, we can extrapolate this information to evaluate the flow rate of the bulk aerosol. Each in-flight image provides the droplet density per unit length (vertical direction) and the corresponding velocity of those droplets. Multiplying this density by the average droplet velocity, we can estimate the total number of droplets that would flow out of the nozzle per unit of time (droplet flow rate). This calculated flow rate can be directly compared to the number of droplets impinged on a substrate per unit of time as verification.

To demonstrate the flow rate calculation of the in-flight imaging system, the flow rates of in-flight and impinged droplets were measured over time. Due to the sparsity of the droplets, and the ability of the algorithm to detect both in-focus and out-of-focus droplets, the imaging system can detect nearly all in-flight droplets. This has been validated by comparing the in-flight flow rate with the impinged flow rate. However, some small droplets may be too dim to be detected in flight. Further research should aim to determine the detection limit in terms of the droplet size in the Mie regime. An area of 710 µm × 100 µm was selected from the impinged images for analysis. This area was chosen to be within a reasonable range of the in-flight droplet column width (93 µm). Droplets outside of this range may be a result of the scattering of dry nanoparticles or post-impingement splashing which could skew the results if included.[30]

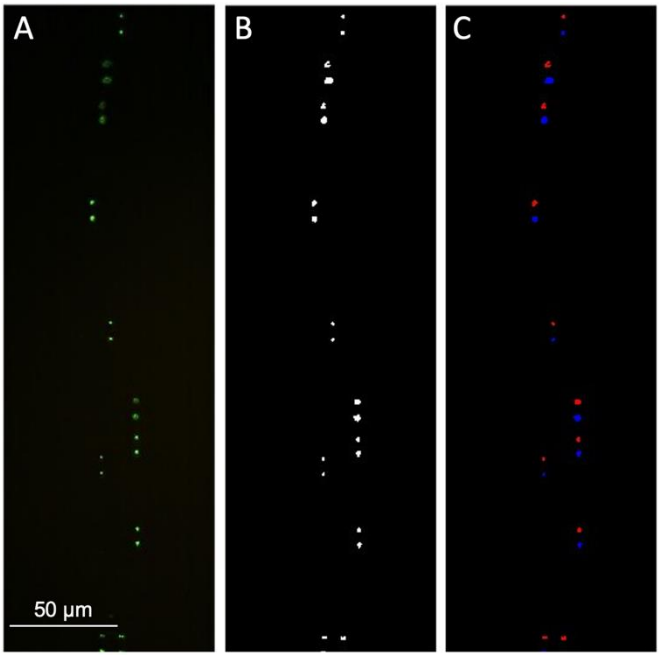

Figure 3. Raw and processed images obtained using the in-flight droplet measurement system including A) raw image, B) binarized image, and C) paired droplets.

A plot of the calculated in-flight droplet flow rate and the measured flow rate based on the impinged droplets is shown in Figure 4. The measurements match very closely over time, displaying similar trends throughout the two-hour experiment. The correlation between both data sets confirms two key factors of our measurement system. First, we can utilize the product of the in-flight droplet density and velocity to accurately monitor the droplet flow rate. Secondly, we show that despite the sparsity of the droplets captured using the laser measurement system, 500 frames are sufficient for predictive measurements.

The time correlation of the flow rate measurements allows for direct insight into the potential causes of variability within AJ printing. In both data sets, the droplet flow rate is shown to decrease between 5–30 min from 200 000–170 000 droplets per second (Figure 4). The decrease in droplet count can be accredited to the loss of large droplets within the transport tube walls. Large droplets have a greater inertia, which counteracts a change in their direction of motion, especially in tighter bends, which increases the probability of impact with the inner walls of the transport tube. As material builds up inside the tube walls, the free space available for droplets to travel through decreases, which results in increased droplet losses.

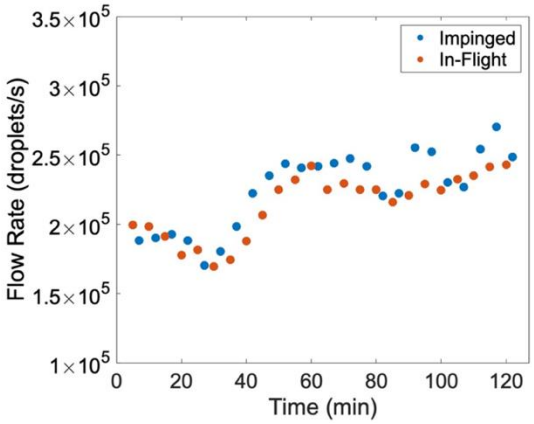

Figure 4. Flow rate of in-flight droplets collected using the laser imaging system and impinged droplets collected using optical microscopy.

The size of aerosol droplets produced through ultrasonication has been shown to decrease over time.[31] Once the droplets reach a sufficiently small size for the inertial forces to reduce, an increase in the droplet flow rate is observed between 30–60 min from 170 000–225 000 droplets per second. Once the system reaches equilibrium, the droplet flow rate levels out from 60–120 min.

3.2 Spatial Dependence of the In-Flight Measurement

To investigate the predictive capabilities of the in-flight measurement system in terms of deposited geometry, lines with various morphologies were printed using focus ratios 0.5, 1, 2, and 4. It has been demonstrated previously that a higher focus ratio results in a narrower aerosol column.[32]

$$Eq.3 \qquad \frac{D_a}{D_N} = \sqrt{1 - \sqrt{\frac{FR}{1 + FR}}}$$

This aligns with the aerodynamic focusing relationship presented in Eq. 3, where the ratio between the aerosol diameter D_a, and the nozzle diameter D_N is given as a function of the focus ratio.[28]

Based on Eq. 3, the selected focus ratios should produce aerosol columns ranging from 65–130 µm. The resulting widths of the deposited lines, the in-flight imaged aerosol column, and the theoretical aerosol column are shown in Figure 5. For all focus ratios, the deposited width is at least 50 µm larger than the in-flight and theoretical aerosol values.

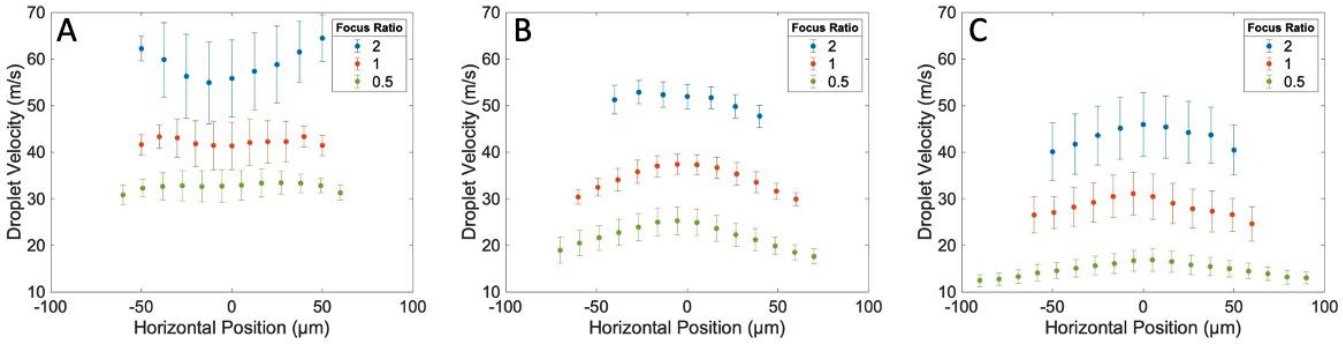

Figure 5. Velocity distribution and standard deviation of imaged droplets A) at the nozzle, B) halfway between the nozzle and the substrate, and C) at the original substrate location (without the substrate present).

All three data sets display the same relationship for focus ratios 0.5–2 where the width decreases steeply for focus ratios 0.5–1 and then decreases more gradually for focus ratios 1–2. The relationship between the focus ratio and the width appears to break down at a focus ratio greater than 2. The large disparity of the focus ratio 4 deposited data set is likely to have been caused by the high sheath gas flow rate inducing droplet drying prior to impingement on the substrate. The drying of the droplets reduces the likelihood of the droplets adhering to the substrate upon initial impact. In addition to this, the reduction in the droplets mass, and consequently reduction in their inertia, decreases their ability to follow the initial flow field, resulting in spreading of the previously collimated aerosol beam.[30] These phenomena are exacerbated by the fluid mechanics associated with the presence of the platen as the theoretical curve ignores the presence of the platen, and the in-flight measurements do not capture the aerosol column's interaction with the platen.

$$Eq.4 \qquad St = \frac{\rho_d C_c d^2 v_d}{18 \mu_d D_N}$$

The Stokes number, shown in Eq. 4, can be used to characterize the flow of the suspended particles where is ρ_d the density of the droplets, C_c is the Cunningham correction factor, d, v_d, and μ_d are the diameter, velocity, and viscosity of the droplets respectively. The median droplet diameter was determined to be 1.7 μm based on an experimental study of the ultrasonic vibration of liquids by Lang.[22] The Cunningham correction factor was evaluated to be 1.1 based on an investigation into particle slip in gases conducted by Davies.[33] The Stokes number was found to be 3.2, 4.3, 5.6, and 6.1 for focus ratios 0.5, 1, 2, and 4 respectively. In theory, a low Stokes number (<<1) results in under-focusing of the aerosol column, and a high Stokes number (>>4) results in over-focusing.[27] The Stokes number is calculated using the assumption that the droplet diameter is constant. However, the droplet diameter decreases with an increase in sheath-gas-induced droplet drying. Therefore, at sufficient focus ratios, the aerosol stream may be under-focused due to a reduction in droplet diameter which could cause significant overspray.

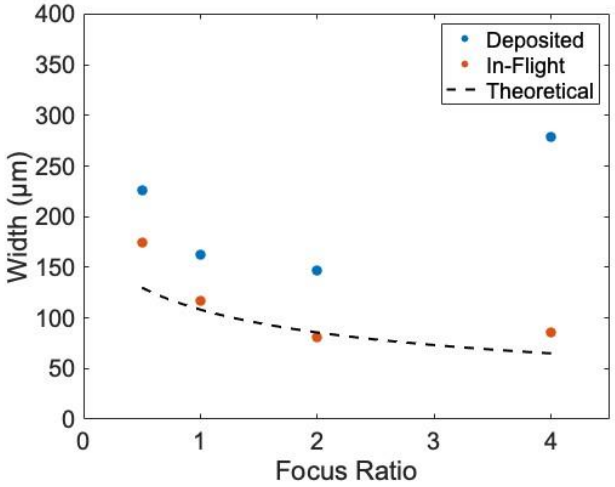

Figure 6. Width of deposited line, in-flight imaged aerosol column, and theoretical aerosol column (Eq. 3) at different focus ratios.

3.3 Velocity Distribution

To further characterize the in-flight measurement systems' ability to provide spatially relevant information, we utilized the technique to observe the spatial dependence of droplet velocities. For this investigation, focus ratios 0.5, 1, 2, and 4 were imaged at three positions between the nozzle and the substrate. Using the information gained in the time-based experiment, both the laser and the printer were primed for 60 min before data collection. Each data set was collected on a separate day for consistency with respect to the prime time and to evaluate the repeatability of the experiments.

3.3.1 Low to Moderate Focus Ratios

Figure 6 shows the effect of focus ratios on the velocity distribution of the droplets at three positions between the nozzle and the substrate. The results demonstrate that there is negligible mixing of the sheath and carrier gas between the deposition head, where the sheath gas is introduced, and the nozzle exit. This is shown by the aerosol stream width being less than the nozzle diameter in all cases. The sheath gas is shown to primarily affect the droplet velocity at the perimeter

of the aerosol column. For focus ratios greater than 1, where the sheath gas flow rate is larger than the carrier gas flow rate, the perimeter of the aerosol column is observed to be traveling at a higher velocity, upon exit of the nozzle, in comparison to the center of the column. In the case where the sheath gas has a lower flow rate compared to the carrier gas (FR = 0.5), the perimeter of the aerosol column is observed to be traveling at a lower velocity, upon exit of the nozzle, in comparison to the center of the column.

As the distance from the nozzle increases, the spreading of the aerosol increases, with the greatest spreading occurring at the lowest focus ratio. This increase in spreading is likely due to the disruption of the aerosol flow field caused by an interaction with the ambient environment, particularly when there is a low flow rate of the protective sheath gas.

3.3.2 High Focus Ratios

Based on the previous results it has been demonstrated that an increase in focus ratio from 0.5–2 results in a decrease in the aerosol column width which is desirable for high-resolution printing. However, this correlation breaks down at larger focus ratios. The same experiment was conducted with a focus ratio of 4 where the overall gas flow rate was 150 SCCM (Figure 7).

$$Eq.5 \qquad \mathrm{Re} = \frac{\rho v D}{\mu}$$

The overall gas flow rate is significant because it affects the Reynolds number of the fluid, shown in Eq. 5, where ρ, v, and μ are the density, velocity, and viscosity of the fluid, and D is the characteristic length. When evaluating the Reynolds number of the gas, the density, velocity, and viscosity of nitrogen should be used with the characteristic length being the nozzle diameter. When evaluating the Reynolds number of the droplets, the density, velocity, and viscosity of the ink should be used with the characteristic length being the droplet diameter. With a Reynolds number of 1045, the gas stream with a focus ratio of 4 is in the transition regime between laminar and turbulent flow.[17] The Reynolds number for focus ratios 0.5, 1, and 2 are 314, 418, and 627 respectively which all fall within the laminar regime.

The same trend as previously reported is observed in the focus ratio 4 data where the velocity at the perimeter of the aerosol stream is directly affected by the flow rate of the sheath gas upon exit of the nozzle, and as the distance from the nozzle increases, the velocity at the perimeter of the aerosol column is most affected. However, with a focus ratio of 4, the average velocity of the aerosol varied greatly between the three positions and did not decrease with an increase in distance from the nozzle as expected. This demonstrates that having a high focus ratio decreases the reproducibility of the aerosol flow field even though the print parameters are consistent.

This inconsistency can likely be accredited to the turbulent flow, which causes mixing of the sheath and carrier gases. In addition to the variation between the experiments, the variation within each experiment was significantly larger compared to the other focus ratios as shown by the large standard deviation. Another discrepancy is that the velocity profile at the substrate is significantly more parabolic compared to the more linear profiles observed with the lower focus ratios. This phenomenon may be caused by the development of eddies at the perimeter of the aerosol stream which would decrease the vertical velocity of the aerosol.[17]

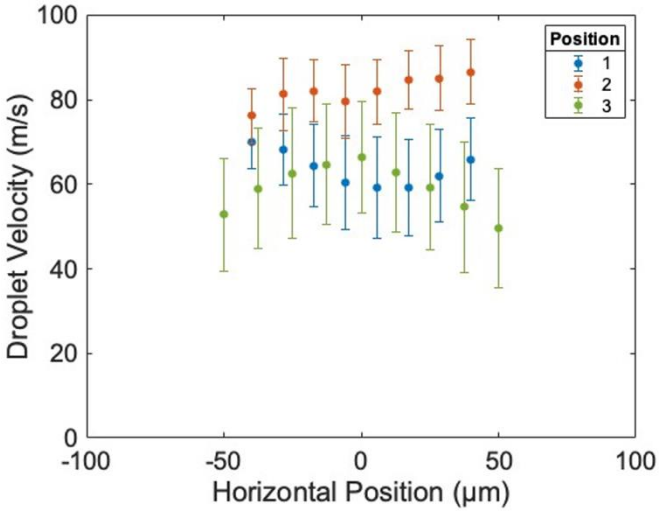

Figure 7. Velocity distribution and standard deviation of imaged droplets with a focus ratio of 4 at the nozzle (Position 1), halfway between the nozzle and the substrate (Position 2), and at the original substrate location (without the substrate present) (Position 3).

3.4 Line morphology

3.4.1 Deposited Lines

The morphology of the printed lines is shown in Figure 8. It is apparent that an increase in the focus ratio from 0.5 to 2 decreases both the overspray and the line width resulting in a higher resolution line. Increasing the focus ratio to 4 decreases the line resolution with an increase in both the overspray and the line width and a decrease in the line height. Through optical profilometry, the line heights of focus ratios 0.5, 1, 2, and 4 were found to be 2.7, 4.7, 5.8, and 1.9 μm, respectively. In addition to the droplet flow rate, the final line morphology is highly dependent on the interaction between the ink and the substrate.

$$Eq.6 \qquad \mathrm{We} = \frac{{v_d}^2 \rho_d d}{\sigma_d}$$

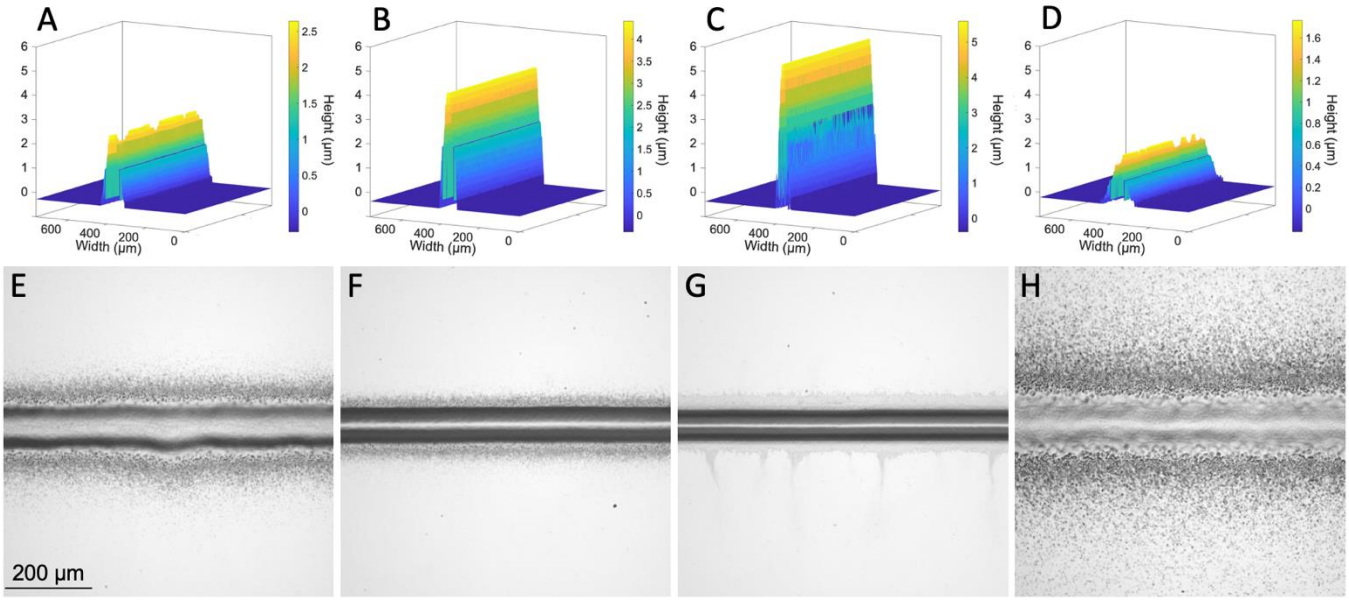

Figure 8. 3-Dimensional deposited line morphology for focus ratios A) 0.5, B) 1, C) 2, D) 4, and 2-dimensional line morphology for focus ratios A) 0.5, B) 1, C) 2, D) 4.

The interaction between the aerosol and the substrate upon impingement can be quantified using the Weber number *We*, shown in Eq. 6, where σ_d is the surface tension of the droplets. The average droplet velocity at a focus ratio of 4 is 61 m s^{-1}. This velocity results in a Weber number of 419 which may lead to a large deformation in the deposited ink. The possible modes of deformation include droplet breakup, droplet spreading, and droplet splashing, all of which contribute to an increase in line width and an increase in overspray.[30] The Weber numbers of focus ratios 0.5, 1, and 2 are 118, 206, and 360 respectively.

$$Eq.7 \qquad \mathrm{Oh} = \frac{\mu_d}{\sqrt{\rho_d \sigma_d d}}$$

$$Eq.8 \qquad \mathrm{K} = Oh \cdot Re^{1.25}$$

According to a study conducted by Mundo *et al.*, the probability of droplet splashing can be evaluated through a correlation between the Ohnesorge (Eq. 7) and droplet Reynolds numbers, where a K value (Eq. 8) greater than 57.7 indicates splashing.[34] The K values corresponding to focus ratios 0.5, 1, 2, and 4 are 19.9, 28.2, 40.0, and 44.0 respectively based on a median droplet diameter of 1.7 μm. However, the droplets are not of uniform size and approximately 10% of the droplets will have a diameter greater than two times the median droplet diameter resulting in K values of 33.5, 47.5, 67.3, and 74.0 for focus ratios 0.5, 1, 2, and 4 respectively.[22] Therefore, droplet splashing is likely at high focus ratios due to the high droplet velocity.

3.4.2 Droplet Flow Rate

To correlate the in-flight droplet measurements to the printed line morphology, the droplet flow rate was quantified as detailed in section 3.1. Assuming that the size variation of the droplets is negligible (or statistically averaged over time), the droplet flow rate can be used as an indicative parameter for the printed line morphology. The droplet flow rate of the in-flight imaged aerosol and the cross-sectional morphology of the printed lines is shown in Figure 9. In both data sets, the ratio between the height and the width increases as the focus ratio increases for focus ratios 0.5–2. The main disparity between the two data sets is that the profiles of the droplet flow rate data are significantly steeper than the profiles of the printed data. As the fluid spreads upon impact and droplet coalescence there is a natural decrease in the aspect ratio of the deposited line. While this substrate-fluid interaction precludes a one-to-one relationship between the droplet flow rate and the deposited line morphology, we hypothesize that for specific ink/substrate combinations, a predictive framework could be developed.

Once a predictive framework is developed, the in-flight flow rate measurement could be utilized as a feedback parameter within a closed-loop control system. The feedback parameter would simultaneously provide real-time data on the aerosol deposition rate and the predicted line geometry for the first time. In future work, we will investigate the transfer function needed to directly utilize the droplet-level flow rate measurements as a fully predictive metric regarding the deposited line profile.

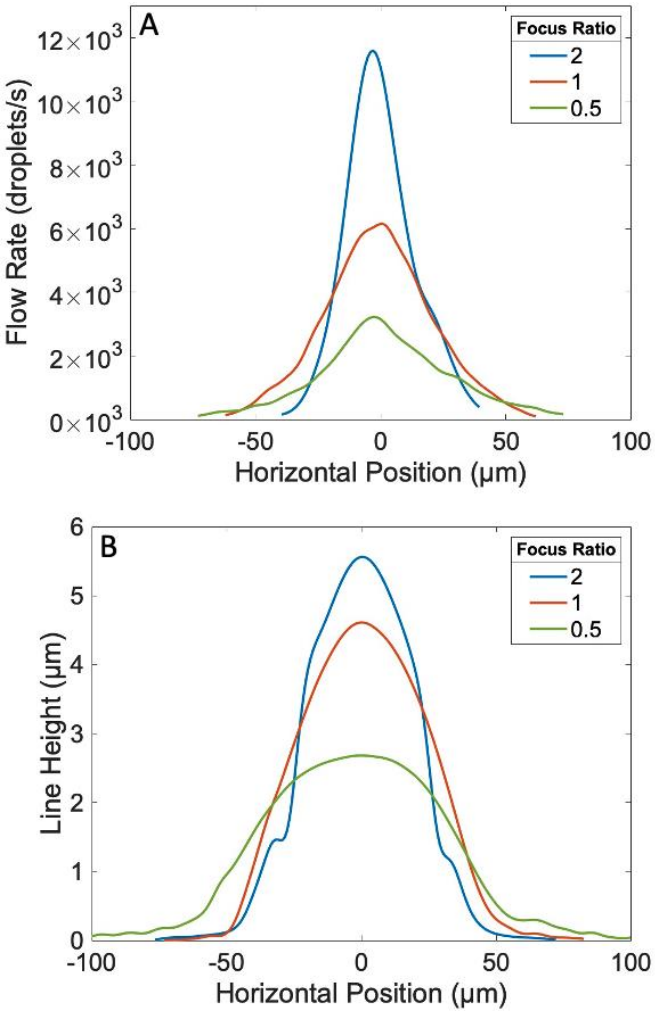

Figure 9. Gaussian-weighted moving average of A) droplet flow rate of the in-flight images droplets, and B) profile of the printed lines collected using optical profilometry.

4. Conclusion

A key limiting factor for aerosol jet printing is the lack of non-invasive feedback to enable closed-loop control. In this work, we investigated the use of a double-pulse optical excitation scheme for providing spatially resolved droplet flow rate measurements. The technique was verified through a direct comparison with impinged droplets, which were deposited discretely during printing. The technique was also able to provide spatial information regarding the aerosol droplet column, with measurements that correlated with theoretically focused column widths. The measured column widths could inform deposited line widths, however, there is a disparity related to the liquid-substrate interaction, and subsequent spreading after impingement. The spatially resolved droplet measurements were extended to allow for direct observation of velocity distributions within the droplet column, allowing for key insights regarding the effect of the sheath gas flow rate on droplets at the edge of the column. At high focus ratios within our setup, we observed inhomogeneities in the flow leading to highly variable droplet velocities and poor impingement properties, including high overspray. These deficiencies can be understood through the calculation of Stokes and Reynolds numbers, ultimately providing experimental evidence of ideal operation windows for printing. Lastly, we demonstrated that the in-flight measurement path provides corollary measures for deposited traces, with future work required to develop a predictive model which can utilize the scheme for closed-loop control. In summary, we present a new technique for measuring in-flight droplets, allowing for new observations and a path toward a non-invasive feedback scheme.

Acknowledgements

We gratefully acknowledge funding support from the University of Wisconsin-Madison's Discovery to Product Center through the Draper Technology Innovation Fund.

References

1. Andersson Ersman, P. *et al.* All-printed large-scale integrated circuits based on organic electrochemical transistors. *Nat Commun* **10**, (2019).
2. Wilkinson, N. J., Lukic-Mann, M., Shuttleworth, M. P., Kay, R. W. & Harris, R. A. Aerosol jet printing for the manufacture of soft robotic devices. *RoboSoft 2019 - 2019 IEEE International Conference on Soft Robotics* 496–501 (2019) doi:10.1109/ROBOSOFT.2019.8722766.
3. Andrews, J. B. *et al.* Printed Electronic Sensor Array for Mapping Tire Tread Thickness Profiles. **19**, 8913–8919 (2019).
4. Fattori, M. *et al.* A Gravure-Printed Organic TFT Technology for Active-Matrix Addressing Applications. *IEEE Electron Device Letters* **40**, 1682–1685 (2019).
5. Yeom, C. *et al.* Large-area compliant tactile sensors using printed carbon nanotube active-matrix backplanes. *Advanced Materials* **27**, 1561–1566 (2015).
6. Cao, X. *et al.* Fully Screen-Printed, Large-Area, and Flexible Active-Matrix Electrochromic Displays Using Carbon Nanotube Thin-Film Transistors. *ACS Nano* **10**, 9816–9822 (2016).
7. Coombs, C. F. *Electronic instrument handbook*. (McGraw-Hill, 2000).
8. Kazemzadeh Farizhandi, A. A., Khalajabadi, S. Z., Krishnadoss, V. & Noshadi, I. Synthesized biocompatible and conductive ink for 3D printing of flexible electronics. *J Mech Behav Biomed Mater* **110**, 103960 (2020).

9. Jansson, E. *et al.* Suitability of Paper-Based Substrates for Printed Electronics. *Materials* **15**, (2022).
10. Yan, K., Li, J., Pan, L. & Shi, Y. Inkjet printing for flexible and wearable electronics. *APL Mater* **8**, (2020).
11. Andò, B. *et al.* Low-Cost Inkjet Printing Technology for the Rapid Prototyping of Transducers. doi:10.3390/s17040748.
12. Lu, S. *et al.* Flexible, Print-in-Place 1D-2D Thin-Film Transistors Using Aerosol Jet Printing. *ACS Nano* **13**, 11263–11272 (2019).
13. Rother, M. *et al.* Aerosol-Jet Printing of Polymer-Sorted (6,5) Carbon Nanotubes for Field-Effect Transistors with High Reproducibility. *Adv Electron Mater* **3**, 1–9 (2017).
14. Agarwala, S., Goh, G. L. & Yeong, W. Y. Aerosol jet printed strain sensor: Simulation studies analyzing the effect of dimension and design on performance (September 2018). *IEEE Access* **6**, 63080–63086 (2018).
15. Lee, S. H., Hwang, J. Y., Kang, K. & Kang, H. Fabrication of organic light emitting display using inkjet printing technology. *ISOT 2009 - International Symposium on Optomechatronic Technologies* 71–76 (2009) doi:10.1109/ISOT.2009.5326101.
16. Tomaszewski, G., Jankowski-Mihułowicz, P., Weglarski, M. & Lichoń, W. Inkjet-printed flexible RFID antenna for UHF RFID transponders. *Materials Science- Poland* **34**, 760–769 (2016).
17. Feng, J. Q. Mist flow visualization for round jets in Aerosol Jet ® printing. *Aerosol Science and Technology* **53**, 45–52 (2019).
18. Salary, R. *et al.* Computational Fluid Dynamics Modeling and Online Monitoring of Aerosol Jet Printing Process. *Journal of Manufacturing Science and Engineering, Transactions of the ASME* **139**, (2017).
19. Williams, N. X., Watson, N., Joh, D. Y., Chilkoti, A. & Franklin, A. D. Aerosol jet printing of biological inks by ultrasonic delivery. *Biofabrication* **12**, (2020).
20. Borghetti, M., Serpelloni, M. & Sardini, E. Printed strain gauge on 3D and low-melting point plastic surface by aerosol jet printing and photonic curing. *Sensors (Switzerland)* **19**, (2019).
21. Hoey, J. M., Lutfurakhmanov, A., Schulz, D. L. & Akhatov, I. S. A review on aerosol-based direct-write and its applications for microelectronics. *J Nanotechnol* (2012) doi:10.1155/2012/324380.
22. Lang, R. J. & Lano, R. J. Ultrasonic Atomization of Liquids. *J Acoust Soc Am* **34**, 6–8 (1962).
23. Tafoya, R. R. & Secor, E. B. Understanding and mitigating process drift in aerosol jet printing. *Flexible and Printed Electronics* **5**, (2020).
24. Lombardi III, J. P., Salary, R., Weerawarne, D. L., Rao, P. K. & Poliks, M. D. Image-Based Closed-Loop Control of Aerosol Jet Printing Using Classical Control Methods. (2019) doi:10.1115/1.4043659.
25. Tafoya, R. R. *et al.* Real-Time Optical Process Monitoring for Structure and Property Control of Aerosol Jet Printed Functional Materials. *Adv Mater Technol* **5**, (2020).
26. Kipman, Y., Mehta, P. & Johnson, K. *Automated Inkjet Print Head Sustainability Testing*. (2010).
27. Secor, E. B. Principles of aerosol jet printing. *Flexible and Printed Electronics* **3**, (2018).
28. Binder, S., Glatthaar, M. & Rädlein, E. Analytical investigation of aerosol jet printing. *Aerosol Science and Technology* **48**, 924–929 (2014).
29. Smith, M., Choi, Y. S., Boughey, C. & Kar-Narayan, S. Controlling and assessing the quality of aerosol jet printed features for large area and flexible electronics. *Flexible and Printed Electronics* **2**, (2017).
30. Chen, G., Gu, Y., Tsang, H., Hines, D. R. & Das, S. The Effect of Droplet Sizes on Overspray in Aerosol-Jet Printing. *Adv Eng Mater* **20**, (2018).
31. Ramisetty, K. A., Pandit, A. B. & Gogate, P. R. Ultrasound assisted preparation of emulsion of coconut oil in water: Understanding the effect of operating parameters and comparison of reactor designs. *Chemical Engineering and Processing: Process Intensification* **88**, 70–77 (2015).
32. Ramesh, S. *et al.* Numerical and experimental investigation of aerosol jet printing. *Addit Manuf* **59**, (2022).
33. Davies, C. N. The Proceedings of The Physical Society Definitive Equations For The Fluid Resistance Of Spheres.
34. Mundo, C., Sommerfeld, M. & Tropea, C. Droplet-Wall Collisions: Experimental Studies of The Deformation And Breakup Process. *Int. J. Multiphase Flow* **21**, 151–173 (1995).